

TOWARD RECONSTRUCTION OF CORONAL MASS EJECTION DENSITY FROM ONLY THREE POINTS OF VIEW

R. A. FRAZIN¹, M. JACOB², W. B. MANCHESTER IV¹, H. MORGAN^{3,4}, AND M. B. WAKIN⁵

¹ Department of Atmospheric, Oceanic and Space Sciences, University of Michigan, Ann Arbor, MI 48109, USA; rfrazin@umich.edu

² Department of Biomedical Engineering, University of Rochester, Rochester, NY 14627, USA

³ Institute for Astronomy, University of Hawaii, 2680 Woodlawn Dr., Honolulu, HI 96822, USA

⁴ Institute for Mathematics and Physical Sciences, Prifysgol Aberystwyth, Ceredigion SY23 3BZ, Wales, UK

⁵ Electrical Engineering and Computer Science Dept., University of Michigan, Ann Arbor, MI 48109, USA

Received 2008 March 12; accepted 2009 January 8; published 2009 April 1

ABSTRACT

Understanding the structure of coronal mass ejections (CMEs) is one of the primary challenges in solar astrophysics. White-light coronagraphs make images of line-of-sight projections of the CME electron density (N_e). The combination of the coronagraphs on the STEREO and SOHO spacecraft provides three simultaneous viewpoints that vary in angle with time, according to the spacecraft orbits. Three viewpoints are not enough to permit tomographic reconstruction via classical methods, but we argue here that recent advances in image processing methods that take into account prior information about the CME geometry may allow one to determine the CME density structure with only three viewpoints. The prior information considered here is that the CME is separated from a known (or simple) background by a closed surface, which may be described by a level set. We propose an alternating iterative procedure in which the surface is evolved via geometric partial differential equations in one step and the interior (and exterior) N_e values are determined in the next step.

Key words: Sun: corona – techniques: image processing

1. INTRODUCTION

One of the great challenges of solar remote sensing is the three-dimensional (3D) reconstruction of coronal mass ejections (CMEs), in which the Sun launches billions of tons of material into interplanetary space. These ejections can damage man-made satellites and threaten astronaut safety, and have even knocked out terrestrial power grids (Webb & Allen 2005). CMEs were first observed in white-light images taken by coronagraphs in the 1970s (see, e.g., Hundhausen 1993 and references therein), and since then their significance for both practical and theoretical reasons has steadily increased. In response to the challenge of understanding the 3D structure of CMEs, NASA launched the dual-spacecraft STEREO mission (Howard et al. 2002). The STEREO mission gives humans the first opportunity to see CMEs from more than one point of view simultaneously. These spacecraft, named “A” for “ahead” and “B” for “behind,” orbit the Sun independently of the Earth, but stay in the plane of the Earth’s orbit. Spacecraft A orbits the Sun every 11.25 months and spacecraft B makes its orbit every 12.75 months. Thus, each spacecraft separates from the Earth by 22° (heliocentric angle) per year. The perspectives of the COR1 and COR2 coronagraphs on the A and B spacecraft (Howard et al. 2002) as well as those of the C2 and C3 coronagraphs on SOHO (Brueckner et al. 1995), which orbits near the L1 Lagrangian point, and the ground-based Mk-IV (Elmore et al. 2003) all combine to give us three simultaneous view angles of the Sun (the views from Earth and L1 are not significantly different for the purposes of this discussion).

Recently, the Extreme UltraViolet Imager (EUVI; Howard et al. 2002) on STEREO has been used to determine the 3D geometry of coronal loops (Feng et al. 2007; Aschwanden et al. 2008). These analyses have assumed that the loops are one-dimensional filaments. Once the same loop has been unambiguously identified in images from both spacecraft, one can use triangulation to find the 3D position of every point

along the loop. Since CMEs are 3D volumetric objects, not one-dimensional filaments, triangulation cannot determine their structure. Frazin & Kamalabadi (2005a) have reviewed 3D tomographic reconstruction of the steady-state corona.

A number of authors have addressed the problem of 3D reconstructions of CMEs in the corona and their interplanetary manifestations (ICMEs). These methods may be categorized by the assumptions they employ about dynamical evolution of the CME. The work presented here is concerned with reconstructing a snapshot of a CME at a time at which three simultaneous coronagraph images are taken with no assumptions about the dynamical evolution, and in that sense it is similar to the (single viewpoint) work of Moran & Davila (2004). They used total brightness (B) and polarized brightness (pB) LASCO-C2 images to find a type of a mean distance of the material for the line of sight (LOS) corresponding to each pixel. Pizzo & Biesecker (2004) developed a method of using LOS intersections from two spacecraft to localize CMEs and determine propagation speeds. Lee et al. (2006) used the correspondence between LOS Doppler shift and spatial position to make a 3D reconstruction of the 2002 April 21 partial halo CME from a time series of UltraViolet Coronagraph Spectrometer (UVCS) spectra taken as the CME drifted past the fixed spectrometer slit. Gapper et al. (1982) were the first to use interplanetary scintillation (IPS) of natural radio sources to model the 3D density structures of the solar wind and ICMEs. In this work, the data were time series of IPS measurements for many sources, and the assumptions of radial flow and constant solar wind speed allowed the authors to find a three-dimensional model that was consistent with the data. Tokumaru et al. (2006) fit a 3D model specified by nine parameters to a set of time-series IPS data in order to follow the interplanetary evolution of the 1999 September 20 halo CME, and this work was followed up with a more sophisticated effort to follow the 2003 October 28 halo CME (Tokumaru et al. 2007). Behannon & Burlaga (1991) combined IPS data with in situ plasma measurements from four spacecraft to map

solar wind stream interactions and transient flows. Howard et al. (2007) analyzed the eruptions of two filaments seen on the disk, and used the observed filament positions to remove the projection effects when the CMEs moved into the LASCO and Solar Mass Ejection Imager (SMEI; Eyles et al. 2003) fields of view (FOV). Jackson et al. (2006) used IPS measurements and SMEI images to make a time-dependent, 3D reconstruction of the heliospheric manifestation of the 2003 October 28 CME by least-squares fitting to a model that assumes the flows propagate radially outward from a source surface. In the future, methods may take advantage of the approximately self-similar evolution of CMEs (Gosling 1999).⁶

Three viewpoints are not enough to permit classical tomographic reconstruction. For example, in medical imaging applications one often has a detector that rotates around the patient taking one or more images per degree of rotation (Kak & Slaney 1987). Previous authors have used solar rotational tomography (SRT) to reconstruct static structures (Altschuler & Perry 1972; Frazin 2000; Frazin & Janzen 2002; Frazin et al. 2007), but the 14 days required to obtain enough view angles are much longer than the hour timescale of dynamic phenomena such as CMEs. Extensions of the classical methods should allow treatment of some mild time-dependent evolution of the corona but not CMEs (Frazin et al. 2005; Saez et al. 2007; Barbey et al. 2008). While in classical tomography one solves for a pixelwise representation of the unknown object (i.e., each pixel of the object is an independent unknown), methods that use other types of representations can be effective in situations in which there is not enough information for classical tomography. Consider a two-dimensional (2D) object living in the plane that is bounded by a closed curve, such that the value of the scene is unity inside the curve and zero outside. One may reconstruct this type of object from a few of its projections, using a curve evolution-based approach (Santosa et al. 1998; Feng et al. 2003). The smooth bounding curve is iteratively evolved using geometric partial differential equations (PDEs), in which the algorithm iteratively modifies the boundary curve until the projections of the reconstructed object match the data. It has been shown that this procedure produces good reconstructions with many fewer viewing angles than would be required for reconstruction via classical tomography methods (Feng et al. 2003). The reconstruction problem is made well-posed by introducing the available prior information to reduce the degrees of freedom. The most important way in which the CME reconstruction problem differs from this simple example is that some CMEs can be assumed to be 3D objects with smooth interiors bounded by a closed surface. We adapt the geometric PDE-based algorithm to the specific problem of CME reconstruction by incorporating this prior information into the model.

2. THE INVERSE PROBLEM

Figure 1 shows a LASCO-C2 image of a CME just after being launched from the Sun's surface. The CME is in the upper left part of the image, and the raylike structures are the background corona. The intensity seen in the j th coronagraph image pixel is given by an LOS integral of the free electron density N_e (van de Hulst 1950):

$$y_j = \int_{-\infty}^{\infty} w(\mathbf{r}_j(l)) N_e(\mathbf{r}_j(l)) dl, \quad (1)$$

⁶ An object that changes in a self-similar manner does not change its shape and its evolution can be described by a time-dependent scale factor.

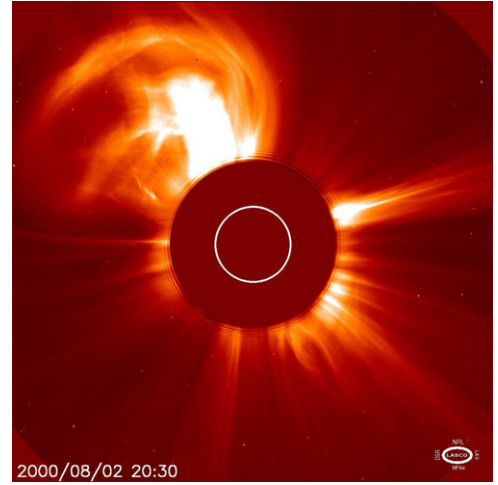


Figure 1. Satellite image of a CME (upper left) superimposed on the background structure in the solar corona. An occulter covers the inner corona and the disk of the Sun that is shown as a white circle. All such images are two-dimensional projections of the corona's complicated three-dimensional structure. Instrument vignetting decreases the large coronal brightness variation from near the Sun to regions more distant from it.

where y_j is the intensity value of the pixel in question, $\mathbf{r}_j(l)$ is a vector that traces the LOS as a function of distance l , and $w(\mathbf{r})$ is a weighting function given by the physics of the Thomson scattering process. The measurement y_j can be the polarized brightness (pB) or the total brightness (B). Using both types of measurements may be useful (Moran & Davila 2004), depending on their relative accuracy (Frazin & Kamalabadi 2005b).

Let the vector \mathbf{f} be a discrete representation of N_e (e.g., each element of \mathbf{f} can represent the value of N_e in a particular volume element of the computation grid). Note that since the \mathbf{f} vector represents a three-dimensional object, it will typically have hundreds or thousands or millions of components. Now consider the vector \mathbf{y} which contains all of the intensity values, i.e., if there are three images each with M pixels, the vector \mathbf{y} will have $3M$ elements. The vector \mathbf{y} is related to \mathbf{f} via:

$$\mathbf{y} = \mathbf{A}\mathbf{f} + \mathbf{n}, \quad (2)$$

where the \mathbf{A} matrix is calculated from Equation (1), and \mathbf{n} represents noise in the data. The vector of electron densities \mathbf{f} exists in a convenient coordinate system, and \mathbf{A} must account for the transformations that relate the coronagraph images to the coordinate system, taking the spacecraft orbital geometry and solar-pole tilt angle into account (Frazin & Janzen 2002).

The reconstruction of the 3D structure of the CME from just three 2D parallel projections (each coronagraph image is a projection) is a highly ill-posed inverse problem made more difficult by a number of factors, including (1) the linear system Equation (2) is either very undetermined and/or has many small singular values, (2) the rapid decrease of intensity with radius in the coronagraph image (due to the Thomson scattering geometry and coronal density fall-off), (3) specification or removal of the background streamer structure (this could be done either in the coronagraph images themselves or in the 3D model space), (4) the complex structure of the CME, and (5) the large density contrast between the shock compressed leading edge and rarefied region behind the shock front.

Some of the challenges one may expect in this 3D reconstruction problem can be appreciated by looking at 3D magnetohydrodynamic (MHD) simulations of CMEs. Such simulations

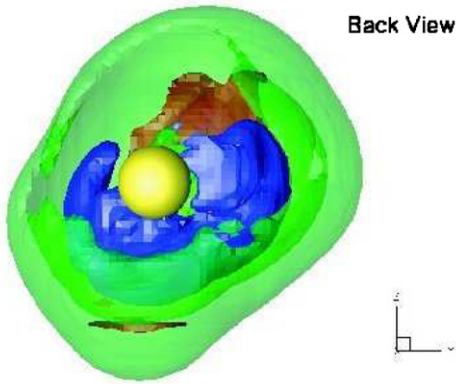


Figure 2. Depiction of the structure of a simulation of the 2003 March 28 CME, viewed from behind the event 15 minutes after initiation, as simulated by Manchester et al. (2008). The yellow ball represents the Sun, the green surface shows the leading shock front, the brown isosurface outlines a region of shock compressed gas, and the blue isosurface outlines a region of rarefaction (also caused by the shock wave).

represent our best guess about the 3D structure of real CMEs, and as an example we use the simulation of the 2003 October 28 event recently published by Manchester et al. (2008). Figure 2 shows a view (from behind the CME) of the simulation 15 minutes after initiation. The yellow ball represents the Sun's surface, and the green surface corresponds to the shock front that precedes the CME. The blue surface outlines the rarefaction region, which has a lower density than the ambient medium. The brown surface shows the region of density enhancement behind the shock front.

The solar corona has a quasi-steady background structure through which the CMEs propagate. The background structures have densities that are comparable to the CMEs and hence are prominent in CME images. This presents an issue for the CME reconstruction, because the CME + background has much more complexity than the CME alone. Figure 3 shows the background corona in projection as seen by the LASCO-C2 (inner portion) and C3 coronagraphs (outer portion). This image has been processed to remove the steep decrease of brightness with radius using methods developed by Morgan et al. (2006). One way to reduce the importance of the background is to subtract pre-event or post-event images from the images that contain the CME eruption. However, this process can introduce errors since the pre- and post-event images can themselves contain transient structures not present at the time of the CME. Figure 4 shows an early stage of the 2003 October 28 CME as seen by C2. The left image has no background subtraction, while the center image has the background from Figure 3 subtracted. The image on the right is synthetic observation based on the simulation of the event by Manchester et al. (2008). The left and center images have been processed with the algorithm by Morgan et al. (2006). While the background subtraction appears to be successful in removing much of the background, the remaining background structure still has some regions comparable in brightness to the CME, and the subtraction process needs to be improved. We note that background subtraction is often used to estimate the masses of CMEs (Vourlidas et al. 2000), but the uncertainty in the CME mass estimate caused by the time-varying background can be large depending on the mass and compactness of the CME. Such masses are in fact only excess mass relative to a presumed stable background. A ejection of coronal mass during a CME incorporates both the outward-moving ambient

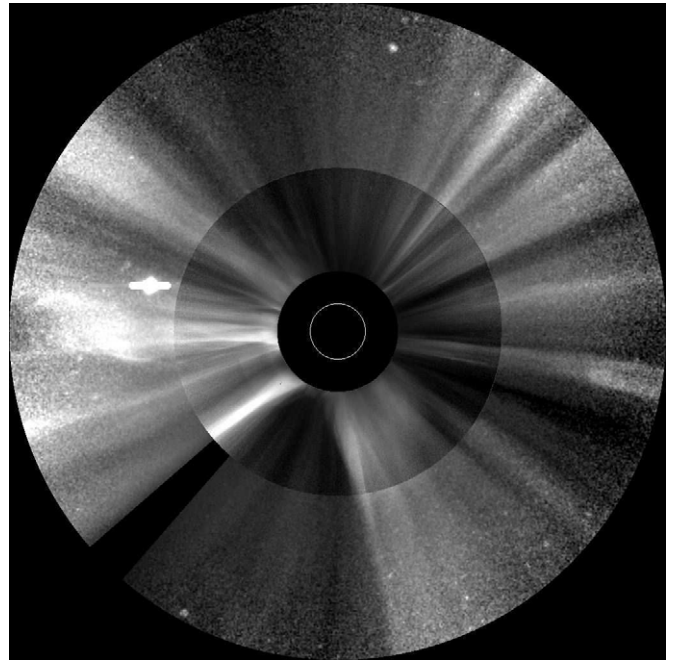


Figure 3. Processed image of the pre-event (background) corona as seen by the LASCO-C2 (inner portion) and C3 (outer portion) coronagraphs on the *SOHO* satellite. A procedure developed by Morgan et al. (2006) removes the steep decrease of intensity with radius so that the structure becomes visible. In the left part of the image, one can see a planet (which saturates the local CCD pixels) and remnants of a previous CME.

and the mass amount that exists in excess during the event. This unknown ambient is not usually included in coronagraph CME mass estimates, since it requires knowledge of the CME volume. Another option is to use SRT to estimate a stable three-dimensional ambient background, but this is again not a direct measurement at the time of the CME.

3. A LEVEL SET SOLUTION METHOD

Since the standard filtered back-projection algorithm (Kak & Slaney 1987) is designed for a large number of projections, it is not useful in this context. Tikhonov (1977) regularized reconstruction (basically, stabilized least squares) is a popular approach to solve ill-posed problems. This scheme assumes a smooth object and reconstructs it from the available projections. This method also fails to provide good reconstructions when only three viewpoints are available. While a Tikhonov scheme would be optimal for a uniformly smooth object, in the CME problem, we assume the object space consists of a localized CME region with a relatively smooth background, with the two regions separated by a closed surface (or curve in the 2D examples given here). We model the object space as being composed of two regions: a smooth background (denoted by \mathbf{f}_2) and a relatively less smooth foreground, which represents the CME (indicated by \mathbf{f}_1):

$$\mathbf{f}_{\text{total}}(\mathbf{r}) = \begin{cases} \mathbf{f}_1(\mathbf{r}); & \text{if } \mathbf{r} \in \Omega \\ \mathbf{f}_2(\mathbf{r}); & \text{if } \mathbf{r} \in \mathbb{R}^2 \setminus \Omega. \end{cases} \quad (3)$$

Here, Ω indicates the foreground region, and \mathbb{R}^2 is the entire object space. The functions \mathbf{f}_1 , \mathbf{f}_2 as well as the boundary of Ω are the unknowns that are estimated from the projection data. The functions \mathbf{f}_1 and \mathbf{f}_2 are supported on Ω and $\mathbb{R}^2 \setminus \Omega$, respectively.

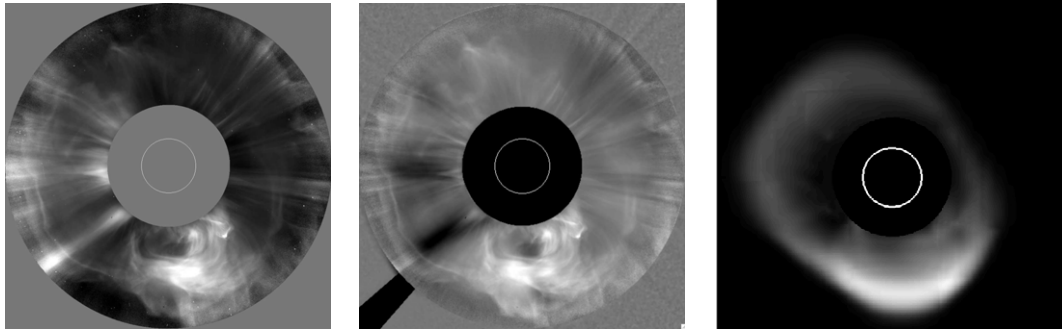


Figure 4. Images of the 2003 October 28 CME without (left) and with (center) the background from Figure 3 subtracted. The image on the right shows a synthetic observation of the MHD simulation of this event, and a quantitative comparison to the measured coronagraph intensities is given in Manchester et al. (2008). The left and center images have radial gradients removed with the technique of Morgan et al. (2006).

See Figure 5 for an illustration. We pose the estimation scheme as an optimization problem:

$$\{\mathbf{f}_1^*, \mathbf{f}_2^*, \Omega^*\} = \arg \min_{\mathbf{f}_1, \mathbf{f}_2, \Omega} \mathcal{C}(\mathbf{f}_1, \mathbf{f}_2, \Omega), \quad (4)$$

where the cost function \mathcal{C} is given by

$$\mathcal{C}(\mathbf{f}_1, \mathbf{f}_2, \Omega) = \underbrace{\|\mathbf{A}\mathbf{f}_{\text{total}} - \mathbf{y}\|^2}_{\text{data-consistency}} + \underbrace{\lambda_1 \int_{\Omega} |\nabla \mathbf{f}_1(\mathbf{r})|^2 d\mathbf{r}}_{\text{smoothness}} + \underbrace{\lambda_2 \int_{\mathbb{R}^2 \setminus \Omega} |\nabla \mathbf{f}_2(\mathbf{r})|^2 d\mathbf{r}}_{\text{smoothness}} + \underbrace{\kappa \int_{\partial\Omega} ds}_{\text{arc-length}}. \quad (5)$$

Here, \mathbf{A} is the operator that maps $\mathbf{f}_{\text{total}}$ onto the projection planes, and \mathbf{y} is the vector of measured intensities (see Equation (2)). The integral $\int_{\partial\Omega} ds$ is the arc length of the boundary of Ω (the boundary is denoted as $\partial\Omega$). The first term in Equation (5) is the data-consistency term, while the second and third terms ensure the smoothness of \mathbf{f}_1 and \mathbf{f}_2 . We choose $\lambda_1 \ll \lambda_2$ so as to ensure a smooth background and a reasonable reconstruction of the foreground. The last term ensures that the boundary of Ω is smooth. Similar to the approach followed in Jacob et al. (2006), we propose to use a two-step iterative algorithm to derive the optimal parameters \mathbf{f}_1^* , \mathbf{f}_2^* , and Ω^* . Starting with an initial guess of $\partial\Omega$, we will derive the optimal \mathbf{f}_1 and \mathbf{f}_2 using the standard conjugate gradient algorithm. In the second step, we update Ω , assuming \mathbf{f}_1 and \mathbf{f}_2 from the previous step. For this step, we represent the region Ω using a level-set scheme and use standard curve evolution schemes (Sethian 1996), which require computational differential geometry, to update $\partial\Omega$. This two-step procedure is repeated until convergence.

Jacob et al. (2006) used a similar approach for the reconstruction of functional activations from near-infrared spectroscopic imaging data of human brain tissue. By assuming the activations to be spatially localized and smooth within the spatial support, the constrained imaging scheme provided much improved reconstructions in comparison to standard methods. The proposed CME reconstruction algorithm is essentially an extension of this scheme.

4. PRELIMINARY RESULTS

To illustrate the appropriateness of the proposed method for the reconstruction of CMEs, we implemented a 2D version of the proposed algorithm. The results are shown in Figure 6. As ground truth, we used a 2D slice of a 3D MHD CME

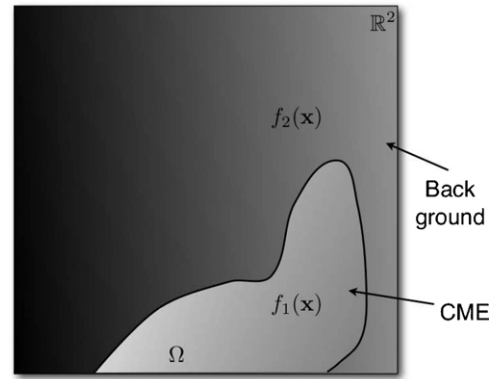


Figure 5. Graphical illustration of the model. The object space is assumed to be composed of two regions: a smooth background and a foreground corresponding to the CME. The foreground region is indicated by Ω , and the boundary curve $\partial\Omega$ separates it from the background. In one step, the algorithm solves for the foreground and background images with $\partial\Omega$ fixed. In the next step, the algorithm modifies $\partial\Omega$, and then the cycle repeats until convergence is achieved. (As illustrated, the boundary curve may intersect the edge of the object space.)

simulation (Tóth et al. 2007; Manchester et al. 2008). The simulation was used to model the 2003 October 28 CME and was shown to reproduce some of the main features of the observed images of this event (Manchester et al. 2008), as in Figure 6. The 2D slice of this simulation was taken at $z = +2 R_s$ (meaning parallel to the Sun’s equator but $2R_s$ above), and it is shown as the left panel of Figure 6. In order to test the new reconstruction process, we calculated line-of-sight projections of the slice for a distant observer at angles (in the plane of the slice) of $(0^\circ(\text{vertical}), 60^\circ, 120^\circ)$. The projections were used as input data to reconstruct the CME using the proposed algorithm (center panel of Figure 6) as well as the standard Tikhonov scheme (right panel). Note the prominent ray-like artifacts (the ray artifacts are along the $(0^\circ, 60^\circ, 120^\circ)$ directions) in the Tikhonov reconstruction. These artifacts are much reduced in our scheme, because it separates the object space into two domains while minimizing the arc length of the curve that separates the domains. Also note that the new reconstruction method does a good job reproducing the boundary of the CME, with the exception of a bump on the left part of the image.

5. CONCLUSIONS

We have argued here that once the background corona can be independently estimated (or eliminated), the blob-like and confined nature of CMEs may allow them to be reconstructed

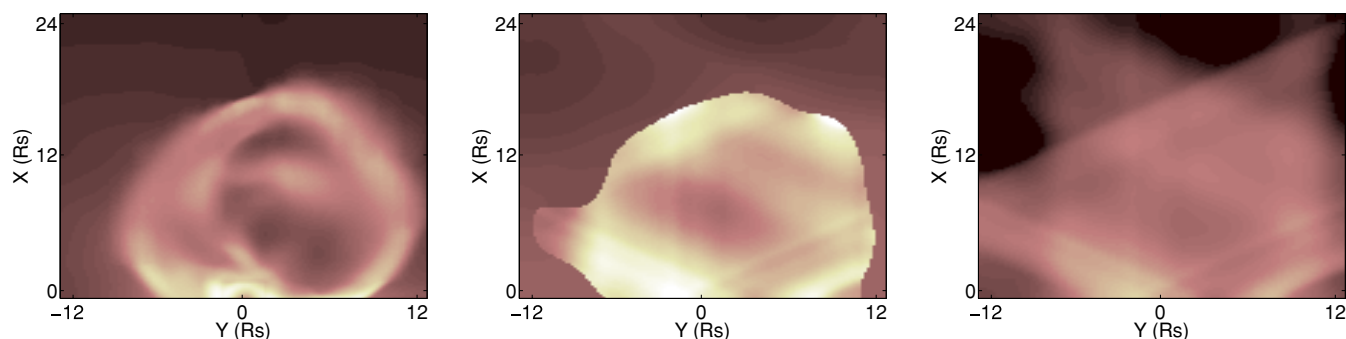


Figure 6. Left: a 2D slice of the simulated 1998 October 28 CME (Manchester et al. 2008) 45 minutes after launch. This slice is taken parallel to the Sun's equatorial plane at $z = +2 R_s$. Center: a reconstruction from three projections at angles of (0° (vertical), 60° , 120°) using our new method. Right: a reconstruction using the standard Tikhonov method. Note that the ray-like artifacts are much reduced when the new method is used and the boundary of the CME is accurately captured, except for a bump on the left edge.

from simultaneous observations at three view angles, which are provided by the *SOHO* and *STEREO* missions. The resulting reconstruction problem cannot be solved via classical methods and must be addressed by more modern image processing methods such as level sets. We described a reconstruction method based on level sets and demonstrated its utility on the reconstruction, from only three view angles, of a 2D slice of a 3D CME simulation. A similar three view-angle situation is provided by the *SOHO* + *STEREO* missions.

We hypothesize that the extension of the level set algorithm to three dimensions will significantly improve the performance. The CME is reasonably smooth along the third (z) dimension, and the use of this information significantly constrains the solutions in the 3D case relative to the 2D case. Given a rapid enough cadence of observations, the situation may improve still further in four dimensions, that is space plus time. In this case, the CME boundary is a smooth 3D surface in four-dimensional spacetime, yielding an even more highly constrained problem. Rathi et al. (2007) proposed a particle filtering method for following the evolution of level-set contours in problems that evolve the tracking of deformable objects. Perhaps a similar methodology may be helpful for finding a the time-dependent surface that separates the CME from the background.

The emerging field of compressed sensing (Donoho 2006; Candès et al. 2006a; Candès & Tao 2006) may offer another alternative to classical tomographic reconstruction methods. The compressed sensing (CS) theory states that an image containing N pixels can be accurately reconstructed from just $M \ll N$ linear measurements,⁷ provided that (1) the image can be expressed as a sparse linear combination of just $K < M/\log(N)$ elements from some basis or dictionary (e.g., wavelet bases), and (2) the linear measurements are collected in a domain that is incoherent with the sparsity-inducing dictionary (for a review of these concepts see Candès & Wakin (2008)). Thus, the CS paradigm is explicitly geared to deal with signal reconstruction from incomplete information. The available linear measurements leave an underdetermined problem (such as Equation (2)) which is solved not by seeking a minimum energy solution (akin to classical techniques), but by seeking an image, subject to agreement with the measurements, whose L_1 norm in the sparse dictionary is smallest. This particular optimization program can be cast as a linear program, and a variety of other formulations have also

been proposed including greedy algorithms (Tropp & Gilbert 2007) and total variation minimization for image reconstruction (Candès & Tao 2006). Again, the problem is made well posed, because the true number of unknowns (the K coefficients in the sparse basis) is less than the number of available measurements; the recovery is also provably robust to measurement noise and extensible to signals that are approximately, but not strictly, sparse (Candès et al. 2006b). Additional models such as manifolds have also been proposed to capture the concise structure present in many real-world signals; these too can be incorporated into the CS paradigm (Baraniuk & Wakin 2009). Some of the earliest experiments in CS demonstrated the dramatic potential for sparsity-based magnetic resonance image reconstruction from highly undersampled Fourier measurements (Candès et al. 2006a). Application of these techniques to CME reconstruction will require the characterization of an appropriate sparsity-inducing dictionary or other concise model for CME images, and the possible development of customized reconstruction algorithms adapted to the particular characteristics of CME coefficients within the dictionary (e.g., Duarte et al. 2008).

REFERENCES

- Altschuler, M. D., & Perry, R. M. 1972, *Sol. Phys.*, **23**, 410
 Aschwanden, M. J., Wuelser, J.-P., Nitta, N. V., & Lemen, J. R. 2008, *ApJ*, **679**, 827
 Baraniuk, R., & Wakin, M. 2009, *Found. Comput. Math.*, **9**, 51
 Barbey, N., Auchère, F., Rodet, T., & Vial, J.-C. 2008, *Sol. Phys.*, in press
 Behannon, K. W., & Burlaga, L. F. 1991, *J. Geophys. Res.*, **96**, 213
 Brueckner, G. E., et al. 1995, *Sol. Phys.*, **162**, 357
 Candès, E., Romberg, J., & Tao, T. 2006a, *IEEE Trans. Inf. Theory*, **52**, 489
 Candès, E., Romberg, J., & Tao, T. 2006b, *Commun. Pure Appl. Math.*, **59**, 1297
 Candès, E., & Tao, T. 2006, *IEEE Trans. Inf. Theory*, **52**, 1206
 Candès, E., & Wakin, M. B. 2008, *IEEE Signal Process. Mag.*, **25**, 21
 Donoho, D. L. 2006, *IEEE Trans. Inf. Theory*, **52**, 1289
 Duarte, M. F., Wakin, M. B., & Baraniuk, R. G. 2008, in Proc. 33rd Int. Conf. Acoustics, Speech, and Signal Processing (ICASSP), (Los Alamitos, CA: IEEE), 5137
 Eyles, C. J., et al. 2003, *Sol. Phys.*, **217**, 319
 Elmore, D. F., Burkpile, J. T., Darnell, J. A., Lecsinski, A. R., & Stanger, A. L. 2003, *Proc. SPIE*, **4843**, 66
 Feng, H., Karl, W. C., & Castañón, D. A. 2003, *IEEE Trans. Image Process.*, **12**, 44
 Feng, L., et al. 2007, *ApJ*, **671**, L205
 Frazin, R. A. 2000, *ApJ*, **530**, 1026
 Frazin, R. A., Butala, M. D., Kembal, A., & Kamalabadi, F. 2005a, *ApJ*, **635**, L197
 Frazin, R. A., & Janzen, P. 2002, *ApJ*, **570**, 408
 Frazin, R. A., & Kamalabadi, F. 2005, *Sol. Phys.*, **228**, 221
 Frazin, R. A., Kamalabadi, F., & Weber, M. A. 2005, *ApJ*, **628**, 1070

⁷ A linear measurement can be modeled by a linear operator acting on the object space. A polarized white-light coronagraph image is an example of a linear measurement.

- Frazin, R. A., Vásquez, A. M., Kamalabadi, F., & Park, H. 2007, *ApJ*, **671**, L201
- Gapper, G. R., Hewish, A., Purvis, A., & Duffet-Smith, P. J. 1982, *Nature*, **296**, 633
- Gosling, J. T. 1999, *J. Geophys. Res.*, **104**, 19851
- Howard, T. A., Fry, C. D., Johnson, J. C., & Webb, D. F. 2007, *ApJ*, **667**, 610
- Howard, R. A., Moses, J. D., Socker, D. G., Dere, K. P., & Cook, J. W. 2002, *Adv. Space Res.*, **29**, 2017
- Hundhausen, A. J. 1993, *J. Geophys. Res.*, **98**, 13177
- Jackson, B. V., Buffington, A., Hick, P. P., Wang, X., & Webb, D. 2006, *J. Geophys. Res.*, **111**, A04591
- Jacob, M., Bresler, Y., Toronov, V., Zhang, X., & Webb, A. 2006, *J. Biomed. Opt.*, **11**, 064029
- Kak, A. C., & Slaney, M. 1987, *Principles of Computerized Tomographic Imaging* (New York: IEEE)
- Lee, J.-Y., Raymond, J. C., Ko, Y.-K., & Kim, K.-S. 2006, *ApJ*, **651**, L566
- Manchester, W. B., IV. 2008, *ApJ*, submitted
- Manchester, W. B., IV, et al. 2008, *ApJ*, **684**, 1448
- Moran, T. G., & Davila, J. M. 2004, *Science*, **305**, 66
- Morgan, H., Habbal, S. R., & Woo, R. 2006, *Sol. Phys.*, **236**, 263
- Pizzo, V. J., & Biasecker, D. A. 2004, *Geophys. Res. Lett.*, **31**, CiteID L21802
- Rathi, Y., Vaswani, N., Tannenbaum, A., & Yezzi, A. 2007, *IEEE Trans. Pattern Anal. Mach. Intell.*, **29**, 1470
- Saez, F., Llebarria, A., Lamy, P., & Vibert, D. 2007, *Astron. Astrophys.*, **473**, 265
- Santosa, F., Litman, A., & Lesselier, D. 1998, *Inverse Probl.*, **14**, 685
- Sethian, J. A. 1996, *Level Set Methods: Evolving Interfaces in Geometry, Fluid Mechanics, Level Set Methods Evolving Interfaces in Geometry, Fluid Mechanics, Computer Vision, and Materials Science* (Cambridge: Cambridge Univ. Press)
- Tikhonov, A. N. 1977, *Solutions of Ill-Posed Problems* (New York: Wiley)
- Tokumaru, M., Kojima, M., Fujiki, K., Yamashita, & Jackson, B. V. 2007, *J. Geophys. Res.*, **112**, A05106
- Tokumaru, M., Yamashita, M., Kojima, M., Fujiki, K., & Nakagawa, T. 2006, *Adv. Space Res.*, **38**, 547
- Tóth, G., et al. 2007, *Space Weather J.*, **5**, S06003
- Tropp, J., & Gilbert, A. C. 2007, *IEEE Trans. Inf. Theory*, **53**, 4655
- van de Hulst, H. C. 1950, *Bull. Astron. Inst. Neth.*, **11**, 135
- Vourlidas, A., Subramanian, P., Dere, K. P., & Howard, R. A. 2000, *ApJ*, **534**, 456
- Webb, D. F., & Allen, J. 2005, *Space Weather*, doi: 10.1029/2004SW000075